UNIVERSITY OF OKLAHOMA

GRADUATE COLLEGE

ELECTRON CONCENTRATION-DEPENDENT OPTICAL PROPERTIES OF INDIUM ARSENIDE

A THESIS

SUBMITTED TO THE GRADUATE FACULTY

in partial fulfillment of the requirements for the

Degree of

MASTER OF SCIENCE

BY

YIXUAN SHEN
Norman, Oklahoma
2023

ELECTRON CONCENTRATION-DEPENDENT OPTICAL PROPERTIES OF INDIUM ARSENIDE

A THESIS APPROVED FOR THE
SCHOOL OF ELECTRICAL AND COMPUTER ENGINEERING

BY THE COMMITTEE CONSISTING OF

Dr. Rui Q. Yang, Chair

Dr. Michael B. Santos

Dr. Zhisheng Shi

Acknowledgements

First and foremost, I would like to express my profound gratitude to my advisor, Dr. Rui Q. Yang, whose attentiveness and dedication are unparalleled. His patience and guidance have been instrumental in helping me overcome challenges and thrive in this field.

I am also profoundly grateful to Dr. Michael Santos and Dr. Zhisheng Shi for serving on my thesis committee. A special acknowledgment goes to Dr. Bin Zheng, whose selfless support has been invaluable. Many times, he listened attentively and provided advice, which has been instrumental in helping me pursue my dream and career goals.

I want to thank my group member, Jeremy Massengale, who has been an indispensable resource in IC fabrication, XRD, and laser measurements. His assistance in establishing a template for filling out the research notebook has greatly facilitated my understanding of the various steps involved. I appreciate his contributions in various aspects. For this thesis, he gives a lot of valuable comments on English writing and the organization of paragraphs. His meticulous and enthusiastic attitude left me a deep impression and encouraged me to be a better researcher. I also want to thank former group members Wenxiang Huang and Yuzhe Lin, who have been generous with their time and expertise in answering my questions and addressing any concerns.

Last but certainly not least, I am deeply indebted to my parents and grandparents for their unyielding understanding and support of my decisions. Their

unconditional love has laid the foundation for my pursuit of higher academic degrees. I am eternally grateful for their encouragement and belief in me.

The research presented in this thesis was supported in part by NSF under Grant ECCS-1931193 and Oklahoma Center for the Advancement of Science & Technology (OCAST) under Award AR21-024.

Table of Contents

List of Tables

List of Figures

Abstract

Since humans began using mirrors to reflect light, its control has been a subject of research for thousands of years. With the use of Maxwell's equations, we came to realize that controlling light is primarily achieved through the manipulation of the refractive index of the material.

Both the real and imaginary parts of the refractive index represent the important optical properties of a semiconductor material. In semiconductors, especially narrow bandgap materials such as InAs, their refractive indices can be significantly modified through manipulation of the material's electron concentration. This has been explored in the development of mid-infrared semiconductor lasers such as quantum and interband cascade lasers (ICLs), which are gaining more and more attention for many applications. Hence, it is important to appropriately evaluate the electron concentration-dependent refractive index in semiconductor materials, which depends on the band structure of the material, for the various semiconductors utilized in such structures.

Previously, many researchers used a simplified two-band $\mathrm{K} \cdot \mathrm{P}$ method to calculate the refractive index of semiconductor materials. However, the results obtained from this two-band model were not systematically compared with other competing models. In this thesis, both a three-band model that includes the spin-orbit split-off band, and the two-band model are used to evaluate the refractive index and compared with experimental results to assess their suitability for three scenarios including plasmon waveguide for ICL, high contrast distributed Bragg reflector(DBR) and reflection measurement.

The results provide a guideline for selecting the appropriate model over different wavelength and carrier concentration ranges for various applications. For a carrier

concentration ranging from 10^{18}cm^{-3} to $3 \times 10^{19}\text{cm}^{-3}$, the three-band model is more accurate. For carrier concentration larger than $3 \times 10^{19}\text{cm}^{-3}$, the two-band model is more accurate. The experimental data also shows some limitations for $\text{K} \cdot \text{P}$ method. The attained results may contribute to the optimization of ICL performance and help other applications like meta-material, resulting in improved device performance and more accurate measurements.

Chapter 1
Introduction

Today, many aspects of our life are based on optical communication, industrial and gas sensors. Because many important gases have their fundamental absorption lines in mid-infrared ($3 \sim 20\,\mu m$) region, semiconductor lasers emitting in the mid-infrared have important applications in gas sensors. However, because of a relatively long wavelength compared to near-infrared (NIR) lasers, making mid-infrared (MIR) semiconductor lasers encounter many technical difficulties. Among various light sources, the interband cascade laser stands out as a superior source for MIR ranges, as will be discussed in the following section.

1.1 The Interband Cascade Laser

1.1.1 History of the ICL

The Interband Cascade Laser (ICL), which was first proposed in 1994 by Rui Yang [1], is desirable for its low power consumption compared to the Quantum Cascade Laser (QCL)[2], [3]. Today, it is a widely used mid-IR semiconductor laser capable of covering a broad range of mid-infrared wavelengths[4], [5]. It is composed of two essential parts: the active cascade region and overall waveguide structure. The cascade active region is composed of three substructures; the hole and electron injectors, and a W-quantum well (QW)[6] active region which takes advantage of the type-II broken-gap. In the W-QW active region, electrons, which are mainly confined within the InAs QWs, recombine with holes that are confined within the $Ga_xIn_{(1-x)}Sb$ layers, resulting in the emission of photons from

this spatially indirect transition. Although wide QWs are typically used for long wavelength or low energy photons, each QW is still only a few nanometers in width. Even with a typical 10 cascade stages, the total thickness of the active cascade region is only a few hundred nanometers (0.1 µm), which is significantly smaller than the emission wavelength (basically from $3 \sim 6$ µm[3], [7], [8], the longest wavelength observed is 13.23 µm based on InAs ICLs[9]). In order to have a large optical confinement with the cascade active region, which serves as the gain medium in the ICL, the various waveguide components are placed on either side of this structure. The SCLs are designed to store optical wave, while the cladding layer is used to confine light.

1.1.2 Optical Waveguides

The thickness of the SCL and cladding layer in an ICL are proportional to the emission wavelength[10], which is usually much larger than the active region. Typically, the SCL in an ICL is formed from undoped or lightly n-doped layers of either GaSb or InAs, depending on the substrate used in the growth (GaSb-based or InAs-based ICL). The traditional cladding layers for the ICL are formed from InAs/AlSb short period (≈ 50Å) superlattices. However, the active region is the only region that provides optical gain, while the SCL and cladding layer can even absorb light. To achieve high-efficiency laser operation with a small threshold current, a low loss, and high optical gain waveguide is necessary. Several improvements are used to achieved through the design of an optimized waveguide structure that confine the light as much as possible within the active region[11]–[13]. A parameter called the confinement factor Γ is used to describe the ability of a waveguide to confine the light to active region.

Γ is determined by the whole waveguide structure, but cladding layer which

are used to confine the light plays a crucial role. Since light prefers to stay in high refractive index materials, a small refractive index in the cladding layer is the key to achieve large values of Γ. The materials used to construct the cladding layer must be lattice-matched to the substrate, which limits the available material choices. Currently, researchers use superlattices, various ternary or quaternary materials, and highly doped semiconductor plasma-enhanced layers to achieve small index cladding layers with a large index contrast with the cascade active region. The acceptable thickness of the cladding layer is determined by the penetration depth of the optical wave, which describes the length that light can penetrate into the cladding layer, and is proportional to the wavelength. Longer wavelengths require thicker cladding layers to prevent light from leaking into the substrate. However, increasing the thickness of the cladding layer also results in more heat accumulation, which can be detrimental to device performance. The reason for this is because the standard InAs/AlSb SL used for the cladding has a low thermal conductivity[14]. For superlattice materials, each layer is only a few nanometers thick, and longer wavelengths require significantly more layers to be grown which also leads to extended growth times an increased number of shutter movements during the MBE growth process, complicating the overall growth.

1.1.3 Plasmon Waveguides

A plasmon-enhanced cladding layer, also called plasmon layer, is a viable solution for ICLs. In earlier reports, ICLs with an InAs plasmon waveguide have demonstrated performance over wavelengths ranging from 4.6 µm to 13.24 µm [9], [11]–[13], [15]–[17]. A plasma layer is a semiconductor layer with high doping level and the refractive index of the layer is controllable with carrier concentration [18]–[20]. According to Drude theory[21], the refractive index of such a material

is highly dependent on carrier concentration and material properties and can approach zero when the emission wavelength is close to the plasma wavelength. This allows us to engineer the index of the material at a specific wavelength. The plasma-enhanced layer has a relatively high thermal conductivity, index contrast, and good confinement. However, the abundance of free electrons in the layer leads to free electron absorption and is a significant optical loss, so optimizing the doping that controls the real and imaginary parts of the index is necessary. The effective mass is an important material parameter in the Drude model and can be derived from the band structure. For many materials, the effective mass can be treated as a constant near the band edge, but for III-V narrow direct bandgap materials, the highly non-parabolic band structure results in wavevector-dependent effective mass.

1.2 Objective of this thesis

Kane's model, which utilizes $\mathrm{K}\cdot\mathrm{P}$ perturbation theory, provides a way to obtain wavevector-dependent effective mass[22]. However, the original function is a cubic equation, making it difficult to use. To overcome this limitation, an approximation has been introduced for specific cases. Although this approximation is not very suitable for InAs, an important material in long wavelength ICLs, researchers still used this approximate model and have achieved results in good agreement with experimental data [23]. The primary focus of this thesis is to assess the accuracy of two models at high doping levels. Specifically, the question is: how accurate are these models? To answer this question, this thesis aims to compare the two models against experimental data. By doing so, a better understanding of the

design of the plasmon cladding layer can be achieved.

This thesis will quantitatively describe the differences that arise from using two different band structure approximations for calculating the refractive index. Chapter 2 will provide a background on the semiconductor parameters related to optical and electrical properties. Two mathematical methods for solving the band structure will also be presented, as they can impact the forementioned properties. Based on these methods, in Chapter 3, numerical results on the carrier concentration and wavelength-dependent refractive index will be presented. Finally, Chapter 4 will summarize the findings obtained throughout the thesis.

Chapter 2
Fundamental Theory

To understand the role that the electron concentration has on the various optical properties of a semiconductor material such as the refractive index, several fundamental theories will be discussed. In section 2.1, the Drude model will be introduced, which connects the electrical and optical properties of the semiconductor. Section 2.2 will discuss the mobility of InAs based on several experimental results. Section 2.3 will present a description of the electron effective mass and its role in band structure theory based on the $K \cdot P$ perturbation method. Finally, in Section 2.4 the band structure and effective mass calculations from two different models will be presented.

2.1 Drude Model

The Drude model, proposed by Paul Drude in a series of papers in 1900[21], assumes the electrons travel freely in crystal with some stationary, heavier crystal ions. This model gives a classic picture elucidates the relationship about the permittivity of a material and its response to an external electric field through the interaction of free electrons. Consequently, the model establishes a connection between electrical properties, such as carrier concentration, and optical properties, including refractive index.

2.1.1 Equation of Motion for electron

When a monochromatic electromagnetic wave, or light, is directed onto a metal, the sinusoidal electric field $\mathbf{E}(t) = \mathrm{E}_0 e^{-i\omega t}$ drives the electrons to move back and forth in an oscillatory motion, where E_0 is the (complex) amplitude of the plane wave, ω is the angular frequency and t is the time; The driving force is the Lorentz force with the frequency of the light ω:

$$\mathbf{F}_\mathrm{d}(t) = -e\mathbf{E}(t) \tag{2.1}$$

where $e = 1.602 \times 10^{-19}$[C] is the elementary charge. The damping force can be represented by a frictional force $\mathbf{F}_\mathrm{r} = m^*\gamma\,\mathbf{v}(t)$ due to different types of collision. Here $\mathbf{v}(t)$ is the velocity of a carrier as a function of time, m^* is the carrier's effective mass, and γ represents the possibility of collisions for carriers with a unit of s^{-1}. The typically range of γ is on the order of $10^{12} \sim 10^{14}[\mathrm{s}^{-1}]$ [24]. Assume there is no restoring force, the equation of motion for a single carriers is given by:

$$m^*\dot{\mathbf{v}}(t) + m^*\gamma\,\mathbf{v}(t) = -e\mathbf{E}(t) \tag{2.2}$$

Since the driving force, which is the electric field $\mathbf{E}$, is sinusoidal, the corresponding electron velocity can be written as:

$$\mathbf{v}(t) = v_0 e^{-i\omega t} \tag{2.3}$$

Where v_0 is the amplitude of the electron velocity. By substituting the expression for $\mathbf{E}(t)$ and $\mathbf{v}(t)$ into Newton's second law equation from Eq.(2.2) allows one to represent the equation of motion in frequency domain. The amplitude of electron velocity v_0 can be derived:

$$v_0 = \frac{eE_0}{m^*(\gamma + i\omega)} \tag{2.4}$$

The current density $\mathbf{J}(t)$ is given by $\mathbf{J}(t) = -Ne\mathbf{v}(t)$, where N is the free electron density with a unit of [cm^{-3}]. By using the above expressions for $\mathbf{v}(t)$ and v_0, one may obtain:

$$\mathbf{J}(t) = \frac{Ne^2}{m^*(\gamma + i\omega)}\mathbf{E}(t) \tag{2.5}$$

The current density $\mathbf{J}(t)$ and electric field $\mathbf{E}(t)$ are related through the material's complex conductivity $\sigma(\omega)$ according to:

$$\mathbf{J}(t) = \sigma(\omega)\mathbf{E}(t) \tag{2.6}$$

Compare with Eq.(2.5) and Eq.(2.6), the formula for complex conductivity $\sigma(\omega)$ is given by:

$$\sigma(\omega) = \frac{Ne^2}{m^*(\gamma + i\omega)} \tag{2.7}$$

The complex permittivity $\varepsilon(\omega)$ is related to the complex conductivity $\sigma(\omega)$ through Ampere's law:

$$\begin{aligned} \nabla \times \mathbf{H} =& \mathbf{J} + \varepsilon_0\varepsilon_\infty \frac{\partial \mathbf{E}}{\partial t} \\ =& \sigma(\omega)\mathbf{E} + \varepsilon_0\varepsilon_\infty \frac{\partial \mathbf{E}}{\partial t} \\ =& -i\omega\varepsilon_0 \left[\varepsilon_\infty + i\frac{\sigma(\omega)}{\omega\varepsilon_0}\right]\mathbf{E} \\ =& -i\omega\varepsilon_0\varepsilon(\omega)\mathbf{E} \end{aligned} \tag{2.8}$$

Where the complex conductivity is defined as:

$$\varepsilon(\omega) \equiv \varepsilon_\infty + i\frac{\sigma(\omega)}{\omega\varepsilon_0} \tag{2.9}$$

Here, ε_0 is the vacuum permittivity $\varepsilon_0 = 8.854 \times 10^{-12}[\mathrm{F\,m^{-1}}]$, and ε_∞ is the high-frequency limit of the permittivity. The high-frequency permittivity limit, ε_∞, represents the relative permittivity of a material at very high frequencies, where the material's response to the electric field becomes negligible compared to its response at lower frequencies. At these high frequencies, the displacement of charges within the material can no longer follow the applied electric field. At this range, the permittivity is related to the background ions. The specific value of ε_∞ depends on the materials (taken as 12.25[10] for InAs).

One may combine the results of Eq.(2.7) into Eq.(2.9) to get expression for complex permittivity $\varepsilon(\omega)$:

$$\varepsilon(\omega) = \varepsilon_\infty - \left(\frac{Ne^2}{m^*\varepsilon_0}\right)\left(\frac{1}{\omega^2 + i\omega\gamma}\right) \tag{2.10}$$

Simplify the expression for $\varepsilon(\omega)$:

$$\varepsilon(\omega) = \varepsilon_\infty \left(1 - \frac{\omega_p^2}{\omega^2 + i\omega\gamma}\right) \tag{2.11}$$

Where ω_p is the plasma frequency which is defined as:

$$\omega_p^2 = \frac{Ne^2}{m^*\varepsilon_0\varepsilon_\infty} \tag{2.12}$$

Eq.(2.11) is the final expression for the complex permittivity $\varepsilon(\omega)$ in the Drude model, which describes the frequency-dependent behavior of conductive materials. Here we can see the plasma frequency is linked with carrier concentration. With controlling the doping, the permittivity of semiconductor can be changed. Because the refractive index is closely related to the permittivity, the materials optical

properties can be manipulated through decent doping.

2.1.2 Refractive index

The complex refractive index $\tilde{n}$ is given by the square root of the complex permittivity:

$$\tilde{n} = n + i\kappa = \sqrt{\varepsilon(\omega)} = \sqrt{\varepsilon_1 + i\varepsilon_2} \tag{2.13}$$

Here, n and κ are the real and imaginary parts of the complex refractive index respectively and ε_1 and ε_2 are the real and imaginary parts of the complex permittivity respectively. From separating the real and imaginary part of Eq.(2.13), n and κ can be given by

$$\begin{aligned} n(\omega) &= \sqrt{\frac{\sqrt{\varepsilon_1(\omega)^2 + \varepsilon_2(\omega)^2} + \varepsilon_1(\omega)}{2}} \\ \kappa(\omega) &= \sqrt{\frac{\sqrt{\varepsilon_1(\omega)^2 + \varepsilon_2(\omega)^2} - \varepsilon_1(\omega)}{2}} \end{aligned} \tag{2.14}$$

For an ideal metal which has a damping of $\gamma = 0$ and conductivity $\sigma = \infty$, the Eq.(2.11) reduces to:

$$\varepsilon(\omega \to \infty) = 1 - \frac{\omega_p^2}{\omega^2} \tag{2.15}$$

Because the imaginary part of the permittivity $\varepsilon_2(\omega) = 0$, the complex part of the index κ vanished and the total index is real. When the optical frequency equals the plasma frequency, the permittivity and the real part of the refractive index is equal to zero. For a non-zero damping, the imaginary part of permittivity is non-zero. Therefore, from Eq.(2.14), the real and imaginary part of the index can close but not equal to zero near the plasma frequency.

The absorption coefficient $\alpha(\omega)$ depends on the imaginary part of index κ

according to:

$$\alpha(\omega) = \frac{4\pi}{\lambda}\kappa(\omega) \tag{2.16}$$

where λ is the wavelength of light in vacuum.

The normal-incidence reflectivity R from air to complex index material can be given by:

$$R = \frac{(n-1)^2 + \kappa^2}{(n+1)^2 + \kappa^2} \tag{2.17}$$

2.2 Electron Mobility

The damping constant in the Drude model characterizes the impeded motion of electrons within the crystal lattice. which comes from several sources:

1. Electron-electron interactions;
2. Electron-lattice interactions;
3. Acoustic phonon interactions;
4. Polar optical phonon interactions.

Those scattering effects that impede the motion of free electrons ultimately convert electric field energy into heat. The damping constant that describes the motion of an electron in a micro-view cannot be measured directly. However, it is related to the mobility, which can be directly measured by the Hall effect, which is a macro-view by the following expression:

$$\mu = \frac{e}{m^* \gamma} \tag{2.18}$$

2.2.1 Caughey-Thomas Mobility Model

The scattering rate of electron due to interactions with other particles is closely related to carrier concentration N. At high carrier concentrations, the scattering rate surges and the electron-electron interaction becomes the dominant factor in scattering. This is particularly relevant for plasma cladding layers, which require a relatively high carrier concentration with an order of $10^{18} - 10^{19}\text{cm}^{-3}$. However, accurately calculating carrier concentration-dependent mobility from multiple scattering rates can be challenging. Instead, many researchers have adopted an empirical mobility model developed by Caughey and Thomas in 1967[25], which has become widely used in the field for calculating the carrier concentration-dependent mobility.

$$\mu(N) = \frac{\mu_{max} - \mu_{min}}{1 + (N/N_{ref})^{\beta}} + \mu_{min} \tag{2.19}$$

Where μ_{max} and μ_{min} are the maximum mobility and minimum mobility at 300 K, respectively, N_{ref} is the carrier concentration when the mobility is reduced to half of μ_{max}, β is a fitting parameters which determines the mobility drop rate. A large value of β leads to a rapid drop, while a small β results in a more gradual decrease. In high carrier concentration when $N \gg N_{ref}$, the the mobility eventually reaches a relatively stable value, where the first term in right hand side of Eq.(2.19) is almost zero and the total mobility is closed to the minimum mobility.

Mobility parameters at 300K	Baranov's parameter
$\mu_{max}[\mathrm{cm}^2\,\mathrm{V}^{-1}\,\mathrm{s}^{-1}]$	30000
$\mu_{min}[\mathrm{cm}^2\,\mathrm{V}^{-1}\,\mathrm{s}^{-1}]$	0
$N_{ref}[\mathrm{cm}^{-3}]$	8×10^{17}
β	0.75

Table 2.1: The mobility parameters for InAs from Baranov[26].

2.2.2 Mobility for InAs

For InAs, there is a set of parameters for the Caughey model given by A. N. Baranov[26] listed in Table 2.1 and plotted in Figure 2.1

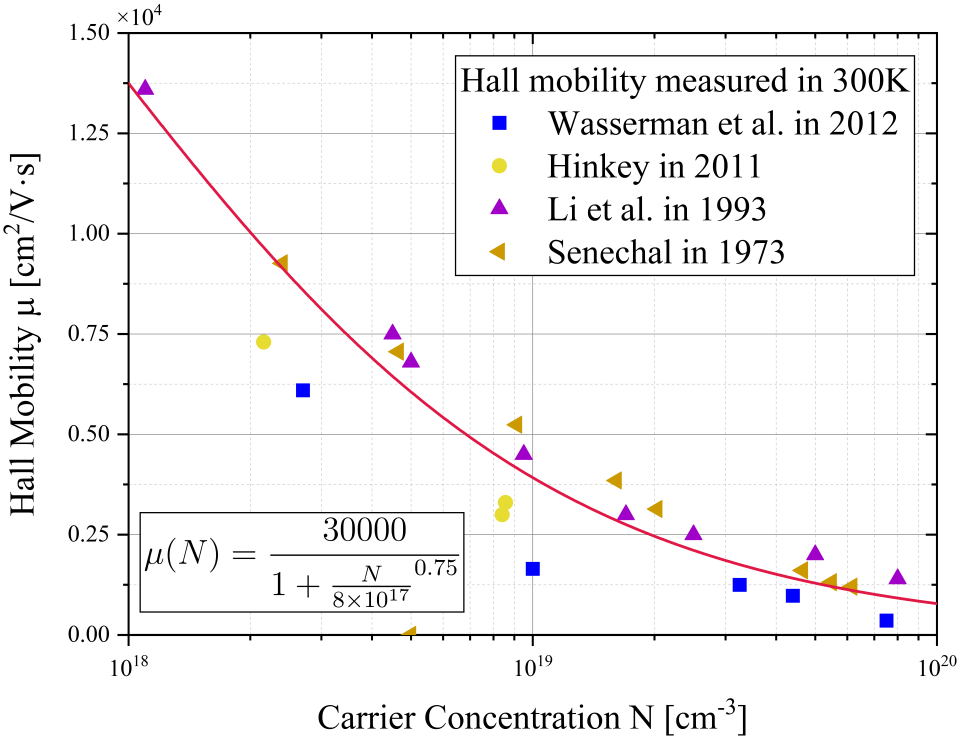

Figure 2.1: The Caughey-Thomas model with Baranov's parameters from $10^{18} - 10^{19}\mathrm{cm}^{-3}$. Also shown are experimentally measured values reported from several groups. [10], [23], [27], [28] All these samples were grown by MBE and measured at 300K.

The carrier concentration in Figure 2.1 varies from $10^{18} - 10^{20}\mathrm{cm}^{-3}$. At this

range, the corresponding plasma wavelength covers from $4 - 15\mu m$, which is sufficient for most mid-IR applications. In Figure 2.1 it is observed that the experimental mobility from Li is slightly higher than the mobility model, while that from Wasserman and Hinkey is slightly lower than experiment data. But the Caughey model using Baranov's parameters still shows a good fit to experiment data.

It worth noting that, at lower temperatures, the mobility is much larger[29] because most scattering rates, for example the phonon scattering, increase strongly with temperature. The change in mobility can have an influence on the refractive index and plasma wavelength. However, for the purposes of this thesis, focus will be solely on the mobility at 300K, and therefore this feature will be ignored. The layer thickness is another important factor that is relevant to the mobility calculated by the Caughey model[30]. However, the details presented here will focus on the calculation of bulk InAs. Because the layer thickness in our applications are thicker enough to be treated as a bulk material.

2.3 Effective Mass and Band Structure Theory

The effective mass is required for calculating the index through the Drude model. The effective mass is closely related to the band structure for non-parabolic materials. Therefore, one must accurately calculate the band structure for the materials of interest, in this case InAs.

2.3.1 Optical Mass

Dirac-like non-parabolic dispersion has been known for narrow bandgap III-V group semiconductors since the mid-1950s. InAs, in particular, is well known for its non-parabolic band structures near band edge, which leads to a small effective mass $m^* = 0.023m_0$ [31] near the band edge. Consequently, the three-dimensional density of states, which is proportional to $(m^*)^{3/2} \times E^{1/2}$, is also small. Here, E is the electron energy. In a highly n^+ doped InAs, free electrons generated by the dopant (Si) can easily fill the bottom of the conduction band and raise the energy. This causes the electron energy and corresponding wavevector dependence on the carrier concentration. The Fermi wave energy E_f and the so-called Fermi vector k_f can be expressed as a function of carrier concentration N:

$$E_f - E_i = k_B T ln \frac{N}{N_i} \tag{2.20}$$

where E_i is the intrinsic energy, N_i is the intrinsic electron concentration, k_B is the Boltzmann constant and T is temperature. For highly doped InAs ($N \sim 10^{19}\text{cm}^{-3} \gg N_i$), the Fermi energy is anticipated to be 100-400 meV above the bottom of the conduction band[10].

Since electrons can only move if there are unoccupied states available, only electrons near the Fermi energy can move freely and participate in transport and optical interactions. Consequently, most optical and electronic properties are associated with electrons at the Fermi energy in high carrier concentrations, or at high temperatures. Eigen states far from the band and the effective mass have to incorporate with non-parabolic effects. The effective mass, which is related to the curvature of the energy bands, becomes Fermi wavevector dependent, leading to the concept of an optical mass [32]:

$$\frac{1}{m^*} = \frac{1}{\hbar k}\frac{dE}{dk}\bigg|_{k=k_f} \tag{2.21}$$

2.3.2 K · P Perturbation Theory

In order to determine the optical mass, the non-parabolic band structure for narrow bandgap III-V materials must be formalized. One of the first and most successful treatments is given by Evan O. Kane who applied K · P theory to InSb[22].

K·P theory is a perturbation theory that describes the energy and wavefunction change for a small perturbation in k-space. According to the Bloch theorem, the electron wave function can be written as $\psi_{nk}(r) = e^{ikr}u_{nk}(r)$, where $u_{nk}(r)$ is periodic with the same periodicity as the direct lattice potential V(r), n represents the electron energy level and k is wavevector. By inserting the Bloch wave function into the Schrodinger wave equation, one may observe:

$$\left[-\frac{\hbar^2}{2m_0}\nabla^2 + V(r)\right]\psi_{nk}(r) = E_n(k)\psi_{nk}(r) \tag{2.22}$$

$$\left[-\frac{\hbar^2}{2m_0}(\nabla^2 + 2ik\nabla - k^2) + V(r)\right]u_{nk}(r) = E_n(k)u_{nk}(r) \tag{2.23}$$

$$\left[-\frac{\hbar^2}{2m_0}\nabla^2 - \frac{\hbar^2}{2m_0}ik\nabla + \frac{\hbar^2k^2}{2m_0} + V(r)\right]u_{nk}(r) = E_n(k)u_{nk}(r) \tag{2.24}$$

$$\left[\frac{p^2}{2m_0} + H' + V(r)\right]u_{nk}(r) = E_n(k)u_{nk}(r) \tag{2.25}$$

where

$$p = -i\hbar k \tag{2.26}$$

$$H' = -\frac{\hbar}{m_0} k \cdot p + \frac{\hbar^2 k^2}{2m_0} \tag{2.27}$$

Where $\hbar = 1.0546 \times 10^{-34}$J s is reduced Planck's constant, $m_0 = 9.1094 \times 10^{-31}$kg is the rest electron mass. Eq.(2.25) represents the general form of $\mathrm{K} \cdot \mathrm{P}$ theory as it applies to a periodic crystal potential. In this equation, H' is treated as a perturbation, with k driving the perturbation. The name of $\mathrm{K} \cdot \mathrm{P}$ perturbation comes from the first term on the right hand side of Eq.(2.27). Due to the nature of perturbation theory, $\mathrm{K} \cdot \mathrm{P}$ theory is only valid for small value of k.

InAs has a zinc-blende structure, in which the bottom of conduction band is s-orbital-like and the tops of the valence bands are p-orbital-like. The atomic bonds of InAs form sp3 hybrid orbitals. When other interactions are not considered, the wave function of the valence bands are threefold degenerated. Where the s-orbital function at k=0 are called: u_s; and p-orbital functions at k=0 are called: $u_x = xf(r), u_y = yf(r), u_z = zf(r)$, where f(r) is a spherical function. The perturbed electron wavefunctions of hybrid orbital can be expressed by linear superposition of orbital functions, which form an orthonormal basis.

$$u_{nk}(r) = Au_s + Bu_x + Cu_y + Du_z \tag{2.28}$$

Where A, B, C and D are coefficients. Substituting equation (2.28) into equation (2.27), since the valence bands are degenerate at k=0, one may find two Eigen energy values, E_c and E_v for the conduction band and valence band respectively. Then multiply $u_i^*, i = s, x, y, z$ on the right hand side; and integrating the function over the space results in four equations. Only when the determinant is zero, is there a meaningful solution for the coefficients.

$$\begin{vmatrix} E_c - \lambda & Pk_x & Pk_y & Pk_z \\ P^*k_x & E_v - \lambda & 0 & 0 \\ P^*k_y & 0 & E_v - \lambda & 0 \\ P^*k_z & 0 & 0 & E_v - \lambda \end{vmatrix} = 0 \tag{2.29}$$

Where $P = -(i\hbar^2)/m_0 \langle U_s|U_i\rangle$ is the momentum matrix element between conduction band and valence bands. Because the valence bands have exactly the same energy, the valence bands is threefold degenerated with three different the wavefunctions. Sometimes, they are simply written as two orthonormal wavefunctions ψ_c and ψ_v for the conduction and valence bands respectively [33].

2.3.3 Spin-orbit Interaction

When the spin-orbit interaction is added, the degenerate valence bands in the four-band model will split into three bands – a light hole band, heavy hole band, and spin-orbit split-off bands. If we consider the electron position as the origin, the ion rotates around the electron. According to Biot-Savart's law, a magnetic field $\boldsymbol{B}$ will be generated by the ion motion. The interaction energy H_{so} comes from the interaction between $\boldsymbol{B}$ and the spin magnetic moment $\boldsymbol{\mu_s} = -e/(m_0)\boldsymbol{\sigma}$, and $\boldsymbol{\sigma}$ is the Pauli spin matrices. With Dirac's relativity theory, the interaction energy can be expressed as

$$H_{so} = -\boldsymbol{\mu_s} \cdot \boldsymbol{B} = \frac{\mu_0}{4\pi}\frac{Ze^2}{m_0^2}\frac{1}{r^3}\frac{\hbar}{2}\boldsymbol{l} \cdot \boldsymbol{\sigma} \tag{2.30}$$

$$\sigma_x = \begin{pmatrix} 0 & 1 \\ 1 & 0 \end{pmatrix}, \sigma_y = \begin{pmatrix} 0 & -i \\ i & 0 \end{pmatrix}, \sigma_z = \begin{pmatrix} 1 & 0 \\ 0 & -1 \end{pmatrix} \tag{2.31}$$

Where Z is the atomic number of the ions, μ_0 is the vacuum permeability and $\boldsymbol{l}$ is the orbit angular momentum defined by

$$\boldsymbol{l} = \boldsymbol{r} \times \boldsymbol{p} = m\boldsymbol{r} \times \boldsymbol{v} \tag{2.32}$$

With the spin-orbital perturbation Eq.(2.30), the equation of $\mathrm{K} \cdot \mathrm{P}$ theory accounting for spin-orbital energy becomes

$$\left[\frac{P^2}{2m_0} + H' + H_{so} + V(r)\right] u_{nk}(r) = E_n(k) u_{nk}(r) \tag{2.33}$$

2.4 Two Band Structure Models

The energy $E_n(k)$ is the eigenvalue of the Schrodinger equation. So, the next step is to solve the equations with and without spin-orbital perturbation.

2.4.1 Three-band Model

The Three-band model includes the spin-orbital perturbation. To solve Eq.(2.33), a spherical polar coordinate basis for wave function are presented by:

$$\begin{aligned} U_s &= u_s \\ U_+ &= -(u_x + iu_y)/\sqrt{2} \\ U_- &= (u_x - iu_y)/\sqrt{2} \\ U_z &= u_z \end{aligned} \tag{2.34}$$

When the spin up $\uparrow$ and spin down $\downarrow$ are considered, there are a total of eight wave functions. Because of the symmetry in the 8×8 matrix, the eight wave

functions can be divide into two groups.

$$\begin{cases} \text{Group A}: & U_s\uparrow, U_+\downarrow, U_-\uparrow, U_z\downarrow \\ \text{Group B}: & U_s\downarrow, U_+\uparrow, U_-\downarrow, U_z\uparrow \end{cases} \tag{2.35}$$

Because of the symmetry, one only need to solve the eigenvalue and eigenfunction for one group. The 4×4 matrix is

$$H_{4\times4} = \begin{bmatrix} E_c & 0 & kP & 0 \\ 0 & E_v - \Delta/3 & \sqrt{2}\Delta/3 & 0 \\ kP & \sqrt{2}\Delta/3 & E_v & 0 \\ 0 & 0 & 0 & E_v + \Delta/3 \end{bmatrix} \tag{2.36}$$

Where Δ is the spin-off energy of the valance band. From equation (2.36), one energy state is decoupled from the other three. This energy band is the heavy hole band. Therefore, this model is subsequently called a three-band model in following. The corresponding eigenvalue can be calculated from

$$E'(E' - E_g)(E' + \Delta) - k^2P^2(E' + \frac{2\Delta}{3}) = 0 \tag{2.37}$$

Where $E'(k) = E(k) - \hbar^2k^2/2m_0$.

Eq.(2.37) is a cubic equation and is hard to solve. Around the band edge, where $k^2P^2 \sim 0$, thus, the solution can be simplified by the first order approximation:

$$
\begin{aligned}
E_c &= E_g + \frac{\hbar^2 k^2}{2m_0} + \frac{\hbar^2 k^2}{6m_0} E_p \left(\frac{2}{E_g} + \frac{1}{E_g + \Delta} \right) \\
E_{hh} &= \frac{\hbar^2 k^2}{2m_0} \\
E_{lh} &= \frac{\hbar^2 k^2}{2m_0} - \frac{\hbar^2 k^2}{3E_g m_0} E_p \\
E_{so} &= -\Delta + \frac{\hbar^2 k^2}{2m_0} - \frac{\hbar^2 k^2}{6m_0(E_g + \Delta)} E_p
\end{aligned}
\tag{2.38}
$$

Where $E_p = 2P^2 m_0/\hbar^2$ has a typically value around 20 eV.

2.4.2 Two-band Model

Under a special case, the cubic equation can be simplified and the three-band model may be reduced to the two-band model [22], [23], [33]. When $\Delta \gg k^2 P^2, E_g$, the influence from the spin-orbital interaction is negligible, Eq.(2.37) can be simplified and the electron energy in the conduction band can be expressed as:

$$
E = \frac{\hbar^2 k^2}{2m_0} + \frac{E_g}{2} \left[\left(1 + \frac{4E_p^2 \hbar^2 k^2}{3m_0 E_g^2} \right)^{1/2} - 1 \right] \tag{2.39}
$$

Because this model is calculated by neglecting spin-orbital split-off valence band , this approximation method is called the two-band model.

2.4.3 E_p for Two Models

E_p can be calculated by expanding the conduction band E_c at band edge where $k \sim 0$:

$$
E_c = E_g + \frac{\hbar^2 k^2}{2m^*(0)} + \vartheta(k) \tag{2.40}
$$

Where $\vartheta(k)$ are higher order corrections. The band structure near the band edge is parabolic and the higher order corrections are ignored. The E_p for three-band

model and two-band model is given by

$$
\begin{aligned}
E_{p-3band} &= E_g \left(\frac{1}{m^*(0)} - 1 \right) \frac{E_g + \Delta}{E_g + 2\Delta/3} \\
E_{p-2band} &= \frac{3E_g}{2} \left(\frac{1}{m^*(0)} - 1 \right)
\end{aligned}
\tag{2.41}
$$

Where $m^*(0)$ is the effective mass at the band edge.

2.5 Numerical calculation for InAs

Li[23] and other researchers used this simplified two-band model for InAs calculations and obtained good results. However, the assumption that $\Delta \gg k^2P^2, E_g$ is not satisfied for InAs with $E_g = 0.354eV$ and $\Delta = 0.39eV$.

The main difference between the three-band model and two-band model is whether the spin-orbit split-off band is included or not. In this section, I am going to quantitatively evaluate and compare how the two models could result in different consequences of predicted band structure and effective mass over a wide range of carrier concentrations.

Parameters	Value
E_g(eV)	0.354
Δ(eV)	0.39
$m^*(0)$(kg)	$0.023m_0$
ε_∞	12.25
$E_{p-3band}$(eV)	18.65
$E_{p-2band}$(eV)	23.06

Table 2.2: Band structure parameters for InAs[34], [35]

In order to calculate the band structure, several basic band structure parameters for InAs at 300K are chosen from Adachi [34] and Levinshtein [35] and listed in Table 2.2. The two E_p values listed in the table are calculated through Eq.(2.41) using parameters from the table.

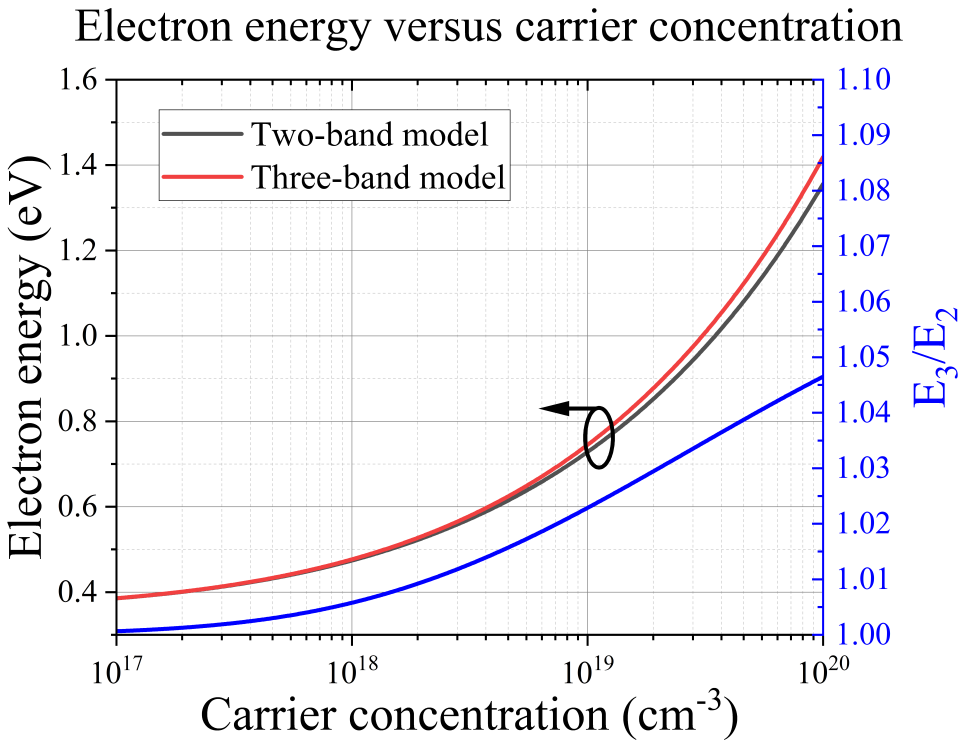

Figure 2.2: The electron energy versus carrier concentration for InAs. The black curve is the band structure calculated from the two-band model and red curve is calculated from the three-band model. The blue curve represents the relative energy difference between the two model.

Figure 2.2 shows a carrier concentration dependent conduction band energy based on three-band model(red) and the two-band model(black). The results demonstrate that the two-band model exhibits lower energy than the three-band model for carrier concentration N greater than 10^{18}cm^{-3}. This discrepancy originates from the spilt-off energy band incorporated in the three-band model, which elevates the light hole band and destroys the threefold degeneracy of the valence bands. The two-band model ignored the split-off band, and has only twofold degeneracy(light-hole and heavy-hole at k=0.). The second term on the right hand side of Eq.(2.39) represents a perturbation term with parameter k. When expanding at $k = 0$, the perturbation term is proportional to k^2 . However, at

high carrier concentration, indicated by a large k value, the perturbation can be simplified to $E_p\hbar k/3m_0$, which contributes less to the rate of energy increase. As a result, the difference between the two band structure models increases more rapidly at high carrier concentrations. Below 10^{18}cm^{-3}, the two models almost overlap. At 10^{18}cm^{-3}, the energy predicted by the two-band model is 0.7% less than three-band model, while the difference increases to 4.7% at 10^{20}cm^{-3}, which is seven times larger.

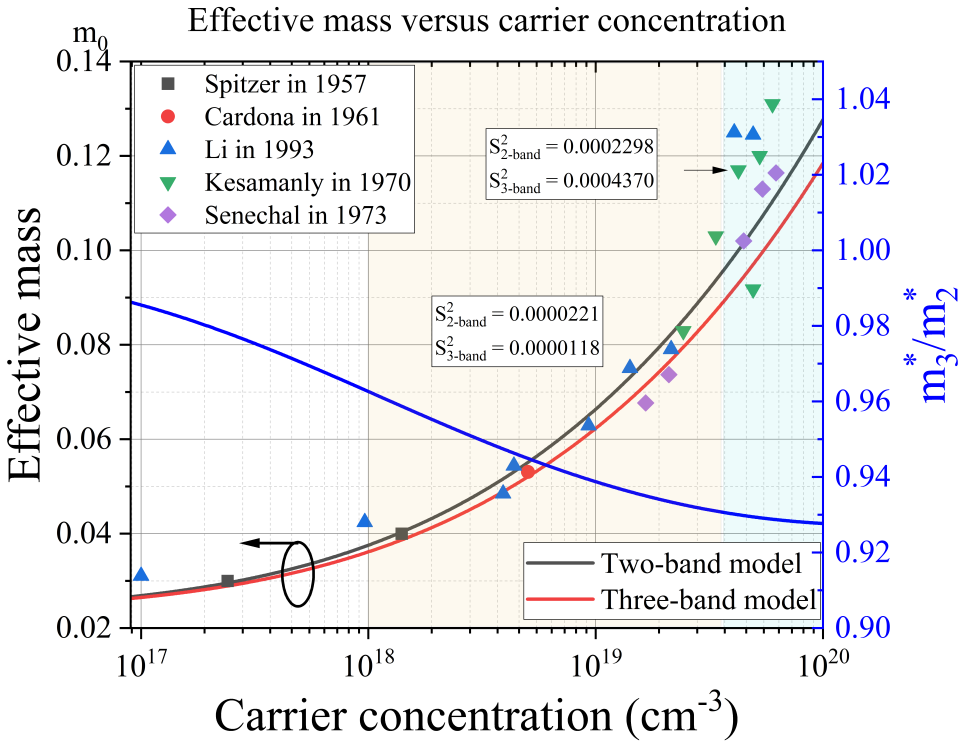

Figure 2.3: The electron effective mass as a function of carrier concentration for InAs. Also shown are experimentally measured values from several groups.[23], [28], [36]–[38] The blue curse represents the relative effective mass difference between the two models.

The variation in band structures directly influences the effective mass because the optical mass from Eq.(2.21) contains the first derivative of the band structure. As a result, the two-band model, which has a modest energy increase rate, presents

a larger effective mass than the three-band model as shown in Figure 2.3. At 10^{18}cm^{-3}, the effective mass calculated by the two-band model is 4% larger than that of the three-band model, while at 10^{20}cm^{-3}, it is 7% larger. This observation aligns with the previous discussion that the perturbation term in the two-band model contributes less to the increase rate, which is the first differential of the band at high carrier concentrations.

Experimental results for effective mass derived from optical measurement are also included in Figure 2.3. For N below 10^{19}cm^{-3}, the experimental data fall between the two models with a variation $S \sim 10^{-5}$. However, when N exceeds $3 \times 10^{19}\text{cm}^{-3}$, the experimental data indicates a much faster increase trend in effective mass than the two models, and the variation increases by a factor of 10. The disparity between the experiment data and the theoretical models shows the limitations of the $\text{K} \cdot \text{P}$ method in dealing with large k-values and high carrier concentrations. The remote band suppression from higher bands is also a contributing factor to this inconsistency. It is worth noting that the remote band contribution becomes more significant at high carrier concentrations, resulting in the breakdown of the $\text{K} \cdot \text{P}$ method. The suppression of remote bands causes a decrease in the energy increase rate, which leads to a heavier effective mass. For low carrier concentrations, denoted by the yellow color in Figure 2.3, the three-band model exhibits a 53.3% smaller variance than the two-band model. However, for high carrier concentrations, denoted by the green color, the three-band model shows a 90.2% larger variance. As discussed earlier, this result indicates that the three-band model provides a better accuracy in low carrier concentrations, while the two-band model performs better beyond $3 \times 10^{19}\text{cm}^{-3}$. Below 10^{17}cm^{-3}, the two models are almost in agreement, but the experiment data shows a larger effective mass than the calculated result.

It is important to note that the experimental data presented in Figure 2.3 are

based on optical measurement and rely on the assumption that the wavelengths at minimum reflection are equal to the plasma wavelengths. However, this assumption is not entirely accurate, as the imaginary part of the index of refraction also contributes to the reflectance R in Eq.(2.17). For a zero-damping system, the minimum reflection is equal to zero when the real index is equal to unity and the frequency $\omega = \omega_p/\sqrt{1 - 1/\varepsilon_\infty}$. The reflection equals one, which indicates the light is completely reflected, when the frequency ω is close to the plasma frequency as the real index is equal to unity. However, when the damping is non-zero, an increase in the imaginary part causes a shift in the minimum reflection, which increases the disparity between minimum reflection frequency and plasma frequency. The frequency shift is related to the high frequency permittivity. For InAs with $\varepsilon_\infty = 12.25$, the measured minimum reflection frequency is typically $3 - 4\%$ higher than the plasma frequency[39], implying that the calculated effective mass in Figure 2.3 may be 7.1% smaller than the actual effective mass. Consequently, the discrepancy between the experimental data and simulation increases in such cases. The reflection changes from one to zero when the frequency only changes 4%. The steep reflection change is called the plasma edge.

In summary, both models are reasonably good when the carrier concentration is below $3 \times 10^{19}\text{cm}^{-3}$, and the three-band model demonstrates a better accuracy between $10^{18} \sim 3 \times 10^{19}\text{cm}^{-3}$. However, when the carrier concentration exceeds $3 \times 10^{19}\text{cm}^{-3}$, a discrepancy arises between the experimental data and the predicted results based on both models. In this range, the two-band model is closer to the experimental data. Nevertheless, it should be noted that the assumption made during the experimental data analysis may lead to a slightly smaller calculated effective mass and a larger discrepancy than that shown in Figure 2.3.

In prior discussions, we established the functional relationship between mobility and carrier concentration via the Caughey model was established; and found the

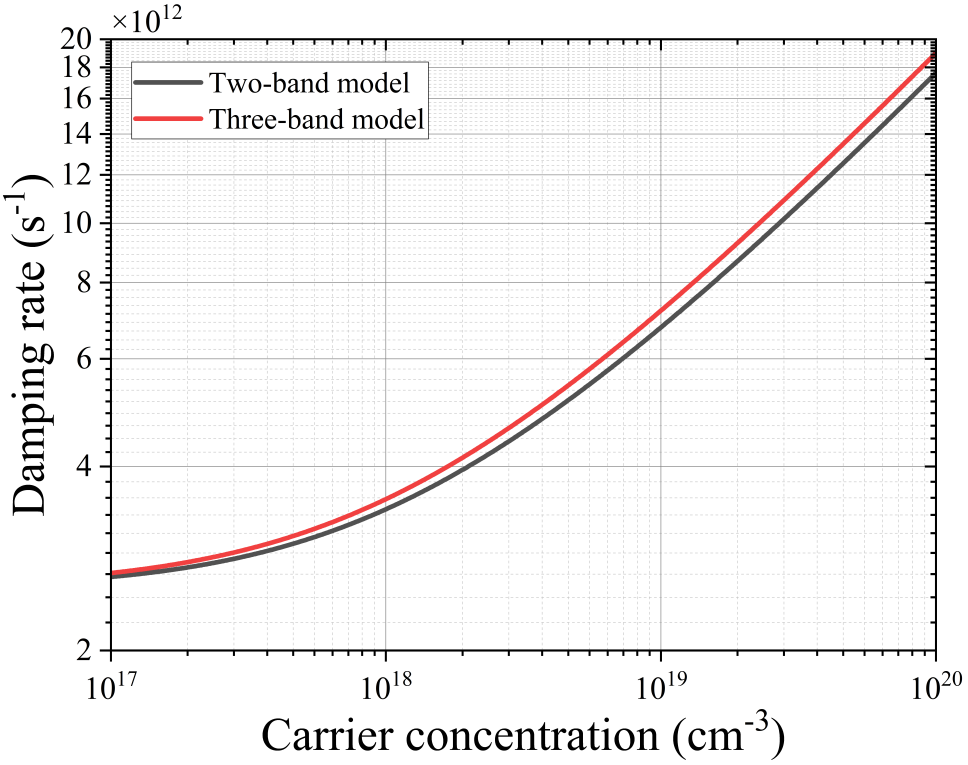

Figure 2.4: Damping versus carrier concentration for the two models.

carrier concentration-dependent effective mass from two band structure models was determined. This lays the foundation for finding the carrier concentration dependent damping, which is a function of mobility and effective mass, by Eq.(2.18). According to this equation, the damping is inversely proportional to both the mobility and the effective mass. As carrier concentration is increased, the increased effective mass will reduce damping; But, at same time, the decreased mobility due to stronger electron-electron interactions will increase damping. As exhibited in Figure 2.4, the overall damping continues to increase with the carrier concentration at high carrier concentrations, despite the interplay between effective mass and mobility. Mathematically, the decrease in mobility due to increasing in carrier concentration is an order of magnitude larger than the increase in effective mass, which finally causes the increasing damping observed in Figure 2.4.

The high damping can be attributed to the higher probability of electron-electron collisions occurring at higher carrier concentrations. As previously discussed, for low carrier concentrations, many collision mechanics play a role in the total collision, but at high carrier concentrations, the carrier-carrier interactions dominate. As shown in Figure 2.4, damping rate increases with the number of carriers. However, Figure 2.3 reveals that both simulation results show an effective mass lower than the experimental data, indicating that the actual damping behavior may not be linear with carrier concentration when the carrier concentration exceeds $3 \times 10^{19}\text{cm}^{-3}$ and may display lower values than those shown in Figure 2.4.

Although both models show an increased damping with carrier concentration, the two-band model exhibits lower damping values. This is because the two-band model has a heavier effective mass than the three-band model, as discussed earlier, resulting in longer electron relaxation times. Consequently, the two-band model demonstrates a lower probability of collisions, leading to lower damping values than the three-band model. Since the effective mass calculated from the two-band model is closer to the experimental data for N exceeding $3 \times 10^{19}\text{cm}^{-3}$, the damping calculated from the two-band model is expected to be more accurate under these conditions, while the three-band model is anticipated to be more accurate when N is below $3 \times 10^{19}\text{cm}^{-3}$.

Chapter 3
Optical Properties Calculated from Two Models

Chapter 2 established the carrier concentration-dependent electrical properties of semiconductor materials including relevant parameters such as the electron mobility, electron energy, and the electron effective mass. We are now ready to explore the effects of these properties on the optical characteristics, such as the refractive index and reflectance. Since the optical properties are also wavelength dependent one should examine the optical properties predicted by the two different models across various wavelengths and carrier concentrations.

3.1 Overview

In this section, a comprehensive overview picture of refractive index, absorption and reflectance for a semiconductor as a function of carrier concentration and wavelength will be provided. The fundamental characteristics discussed here will be further explored under specific applications in the next section.

3.1.1 Refractive index and Absorption

Using the calculated results for the band structure and effective mass from Chapter 2, the refractive index can be calculated as a function of the carrier concentration and optical wavelength.

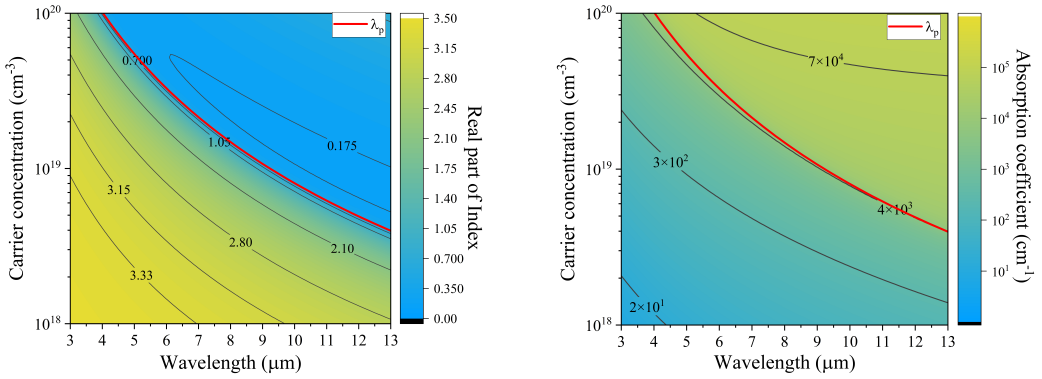

(a) Real part of refractive index (b) Free carrier absorption

Figure 3.1: Real part of refractive index and free carrier absorption as a function of carrier concentration and wavelength based on the three-band model. The red curve represents the calculated plasma wavelength as a function of carrier concentration.

Figure 3.1 shows the calculated real part of the refractive index (a) based on Eq.(2.14) and the free-carrier absorption (b) based on Eq.(2.16) over a large carrier concentration range ($10^{18} \sim 10^{20}$cm^{-3}) for InAs using results obtained from the three-band model. In this figure, the red line represents the plasma wavelength in air calculated from Eq.(2.12). Both the index and absorption coefficient have a substantially change when across the plasma wavelength.

As illustrated in Figure 3.1a, in the region above and to the right of the red curve constitutes a regime where the index is low, which results in a corresponding region in Figure 3.1b where the absorption coefficient is high. Similarly, in regions below the red curve in Figure 3.1a, the real part of the refractive index is high and the corresponding free-carrier loss is low (Figure 3.1b). This indicates that the real part of the refractive index, the so called index below, and the absorption coefficient exhibit significant changes around plasma wavelength. This lead to a trade-off between the optical confinement and free carrier loss which must be accounted for when designing appropriate optical applications, such as the ICL waveguide.

3.1.2 Reflection

The changes in the real and imaginary part of the refractive index around the plasma frequency consequently lead to a significant variations in reflection, demonstrated in Figure 3.2. The orange region represents high reflectance approaching 100% for highly doped structure at longer wavelengths. The blue curve indicates the location of reflectance minimum just below the plasma wavelength. As mentioned in Chapter 2, the reflection undergoes a rapid change from zero(or a minimum with nonzero damping) to nearly 100% when the optical frequency from a high end crosses the plasma frequency. This phenomenon is known as the plasma edge[10], which plays an important role in material properties measurement.

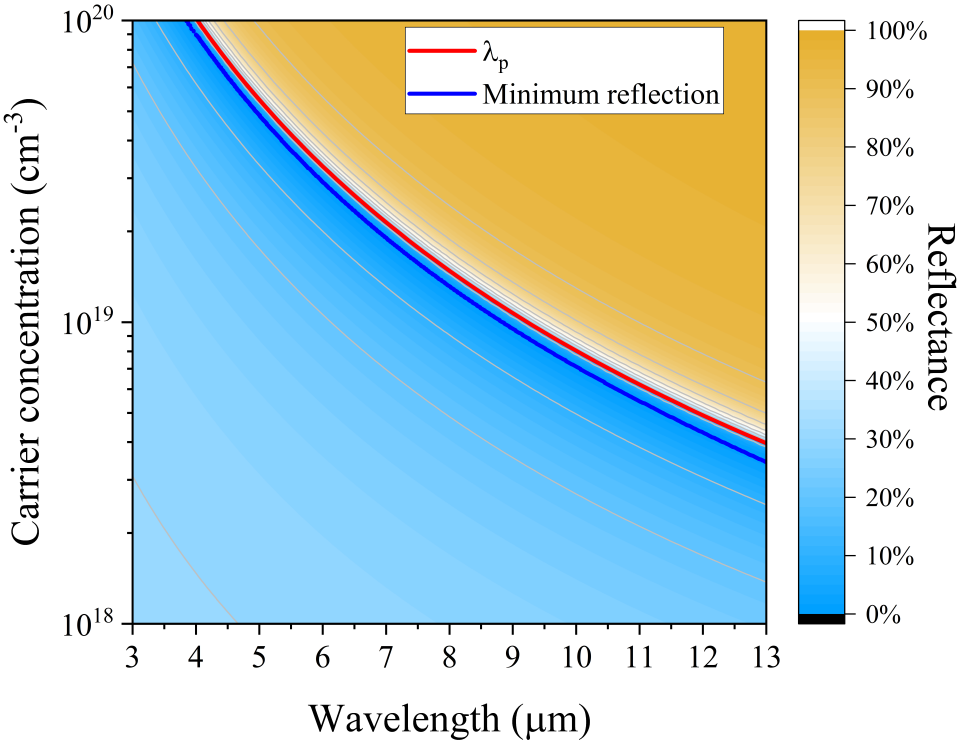

Figure 3.2: Reflectance for InAs as a function of carrier concentration and wavelength based on three-band model.

If the doping concentration and plasma frequency are known, the effective mass

can be extracted from the plasma frequency using Eq.(2.12). Experimentally, the plasma frequency can be obtained by finding the plasma edge. The plasma edge and minimum reflection wavelength can be used as a guide to calculate the plasma frequency and effective mass of carriers in a semiconductor. This is an essential non-destructive method in semiconductor research.

The frequency corresponding to minimum reflection does not equate exactly to the plasma frequency. Suppose we want to determine the effective mass through the plasma wavelength, with a carrier concentration determined by Hall measurement. In Figure 3.2, for an identical doping level, the wavelength corresponding to the minimum reflection λ_{min} (Blue curve) always exhibits a smaller value than the wavelength corresponding to the plasma wavelength λ_p. If assuming the plasma frequency is λ_{min}, the smaller wavelength eventually leads to a higher carrier concentration and heavier effective mass. Thus, the effective mass determined by the minimum reflection wavelengths is larger than that determined by the actual plasma frequency [40]. The deviation is associated to high frequency limit permittivity ε_∞ and damping γ. When the value of γ is large, the ratio between the plasma frequency and the minimum reflection frequency $\omega_p/\omega_{min} = 1.05\%$ for InAs with $\varepsilon_\infty = 12.25$ [41]. It can be observed in Figure 3.2 that for $\lambda = 8\mu m$, the carrier concentrations calculated from the minimum reflection frequency are approximately 13% smaller than those derived from the plasma frequency.

3.2 Two models in different applications

When incorporating the concept of carrier-concentration controlled refractive index into various optical applications, several distinct conditions must be considered. For instance, ICL have a designated emission wavelength and necessitate determining an appropriate doping level to optimize threshold gain. Different applications will require specific performance evaluations based on their unique conditions. In this section, the optical properties will be viewed from different perspectives for three applications and discuss how to selecting the appropriate model based on their own conditions.

3.2.1 ICL Waveguide Design

For an ICL plasmon waveguide design with a specific target wavelength, the goal is to determine the optimized carrier concentration to minimize the threshold gain. An accurate real index and absorption model are required to reduce the free carrier loss and enhance the confinement. The carrier concentration dependent index and absorption for InAs at 300K are plotted in Figure 3.3 for three different wavelengths($3.3\mu m, 6\mu m$ and $10\mu m$) using both the two-band model(dashed) and the three-band model(solid). Also shown are the calculated absorption coefficients for each wavelength, based on the two models.

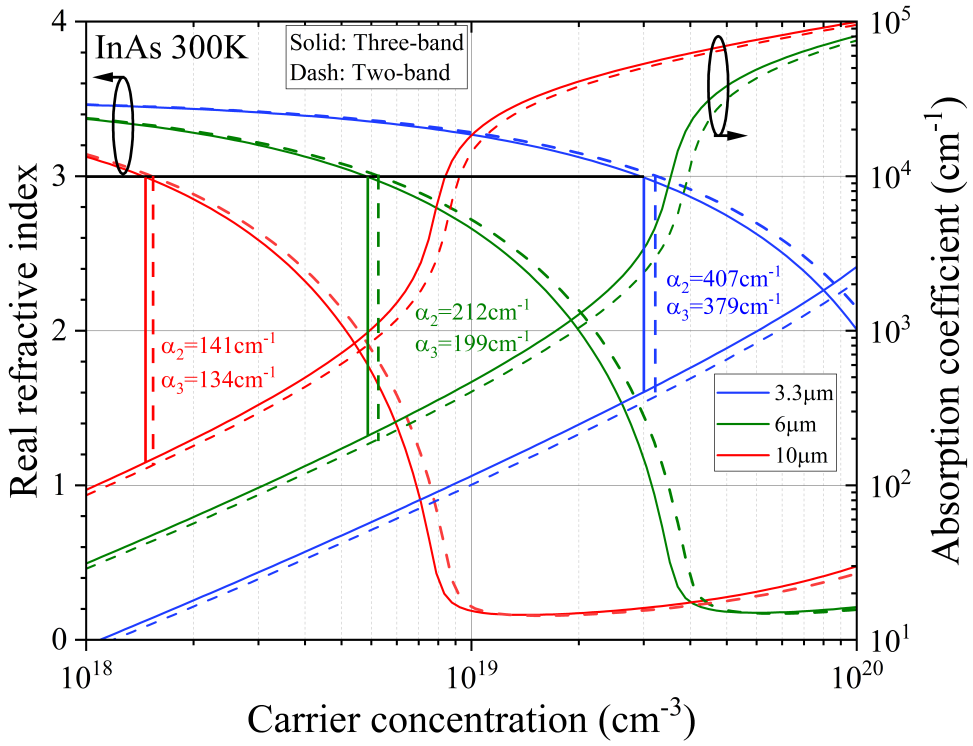

Figure 3.3: InAs refractive index and absorption coefficient as a function of carrier concentration for different wavelengths.

As shown in the figure, the three-band model consistently exhibits a slightly smaller index and larger free carrier absorption for specific carrier concentrations, which makes sense as the imaginary part of the refractive index is larger according the three-band model. The real index directly influences on the confinement factor. Assuming the same real index yields the same confinement, for an index that is equal to 3 (black horizon line in Figure 3.3), higher carrier concentrations are required to achieve the same confinement at shorter wavelengths. At the same time, the free carrier absorption increases with the carrier concentration. Consequently, designing cladding layers for short-wavelength ICLs may be more challenging due to higher absorption. The highest doping that can achieve is around 10^{20}cm^{-3}, which becomes the limitation for InAs plasma cladding layer for short emitting wavelength below 3μm.

For the same wavelength, in order to achieve an index of n=3, the predicted carrier concentration required based on the the two-band model is larger. This is due to the larger effective mass calculated from the two-band model than that from the three-band model, resulting in a higher plasma frequency and larger carrier concentrations. When $N = 1.05 \times 10^{18}\text{cm}^{-3}$, the absorption coefficient from the two-band model $\alpha_2 = 141\text{cm}^{-1}$ and from the three-band model $\alpha_3 = 134\text{cm}^{-1}$ for $\lambda = 10\mu\text{m}$ with a refractive index =3. The relative absorption coefficient difference is 5.2%. When $N = 5 \times 10^{18}\text{cm}^{-3}$, $\alpha_2 = 212\text{cm}^{-1}$ and $\alpha_3 = 199\text{cm}^{-1}$ for $\lambda = 6\mu\text{m}$ with index =3. The relative absorption coefficient difference is 6.5%. When $N = 2 \times 10^{19}\text{cm}^{-3}$, $\alpha_2 = 407\text{cm}^{-1}$ and $\alpha_3 = 379\text{cm}^{-1}$ for $\lambda = 3.3\mu\text{m}$ with index =3. The relative absorption coefficient difference is 7.3%. Therefore, the absorption coefficient calculated by the two-band model is larger than that of the three-band model for same index; and the disparity increases with higher carrier concentrations due to the growing effective mass disparity between the two models. At a low carrier concentration, both band models are good enough. However, the two-band model provides a more accurate effective mass at high carrier concentrations, thus, the index and absorption coefficient from the two-band model are also more appropriate for $N > 3 \times 10^{19}\text{cm}^{-3}$.

On the other hand, at the same carrier concentration, the absorption coefficient obtained from the three-band model with a smaller electron effective mass is higher than that from the two-band model, while the refractive index is lower. This may result in an overestimated threshold gain from the three-band model especially when the carrier concentration is high. This is because, in Figure 2.3, both band models show a relatively large disparity from experimental data for $N > 3 \times 10^{19}\text{cm}^{-3}$. The experimental data indicates a larger effective mass, implying a lower plasma frequency according to Eq.(2.12), a higher index and a lower absorption coefficient than the simulation result for a high carrier concentration. Therefore, in order

to achieve the same confinement in the active region of a laser operating at a short wavelength, a higher doping is required, which may increase the free-carrier absorption.

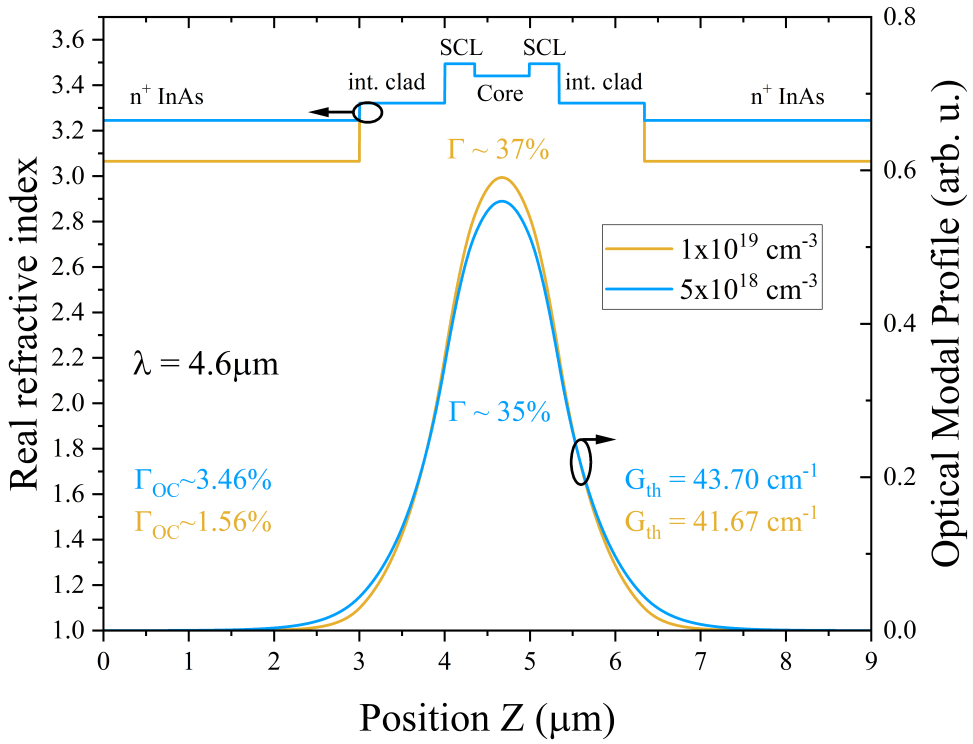

Figure 3.4: The calculated optical modal profile and refractive index for an InAs plasmon cladding ICL with an emission wavelength of $\lambda = 4.6\mu m$. All calculations are based on the two-band model. The blue and orange curve represent the wave profile of ICL for a cladding layer with carrier concentration $N = 5 \times 10^{18} cm^{-3}$ and $1 \times 10^{19} cm^{-3}$ respectively. The cavity length is assumed to be 1.5mm.

Figure 3.4 presents a calculated optical modal profile and refractive index based on the two-band model for a simplified InAs-based plasmon waveguide ICL with a designed emission wavelength of $\lambda = 4.6\mu m$. The core region lies at the center of the ICL, sandwiched by two InAs SCLs, each with a thickness of 0.35μm. Outside of the SCLs are placed intermediate cladding layers composed of InAs/AlSb short period SLs, each with a thickness of 1μm; and n^+ doped InAs plasmon cladding layers located at the outermost sections of the waveguide, with

a thickness of 3µm at both sides. The blue and orange curves represents the different carrier concentrations for the InAs plasmon layers. At $N = 10^{19}\text{cm}^{-3}$, represented by the orange curve, the real index of the InAs plasmon cladding layer is substantially lower than that at $5 \times 10^{18}\text{cm}^{-3}$. Consequently, the cascade active region confinement Γ is larger and the optical light intensity Γ_{oc} in the outside cladding layer is lower. Although the free carrier absorption increases rapidly, the required threshold gain for the ICL slightly decreases. This can be attributed to the competition between the increasing confinement factor and absorption coefficient.

Changing the carrier concentration of both n^+ doped InAs cladding layers at top and bottom while keeping the rest of the ICL structures the same leads to changes in the threshold gain. The complex index that changes in the plasmon cladding layer will affect the active region confinement and the absorption coefficient in the plasmon layer. Table 3.1 presents the threshold gain calculated using the two models at three specific carrier concentrations, and the threshold gain results are plotted in Figure 3.5

N $[\text{cm}^{-3}]$	α_{3band} $[\text{cm}^{-1}]$	$G_{th-3band}$ $[\text{cm}^{-1}]$	Γ_{3band}	α_{2band} $[\text{cm}^{-1}]$	$G_{th-2band}$ $[\text{cm}^{-1}]$	Γ_{2band}
5.0×10^{18}	105.1	43.66	35.10%	93.4	43.70	34.83%
8.0×10^{18}	183.1	42.22	36.40%	160.8	42.09	36.20%
1.0×10^{19}	240.5	41.88	36.87%	209.8	41.67	36.70%
1.5×10^{19}	402.3	41.53	37.58%	346.7	41.27	37.44%
1.8×10^{19}	512.5	41.49	37.86%	438.8	41.18	37.73%
2.0×10^{19}	591.9	41.47	38.00%	504.7	41.17	37.88%
2.2×10^{19}	676.4	41.48	38.13%	574.3	41.15	38.01%
2.5×10^{19}	813.6	41.5	38.30%	686.3	41.16	38.18%
3.0×10^{19}	1074	41.57	38.51%	895.4	41.21	38.40%
5.0×10^{19}	2841	41.93	39.04%	2180	41.50	38.95%

Table 3.1: The simulation results for InAs plasmon waveguide ICL. The emission wavelength is 4.6µm and cavity length is 1.5mm

From the discussion for Figure 3.3, at the same carrier concentration, the three-band model exhibits a relatively higher free carrier loss and confinement

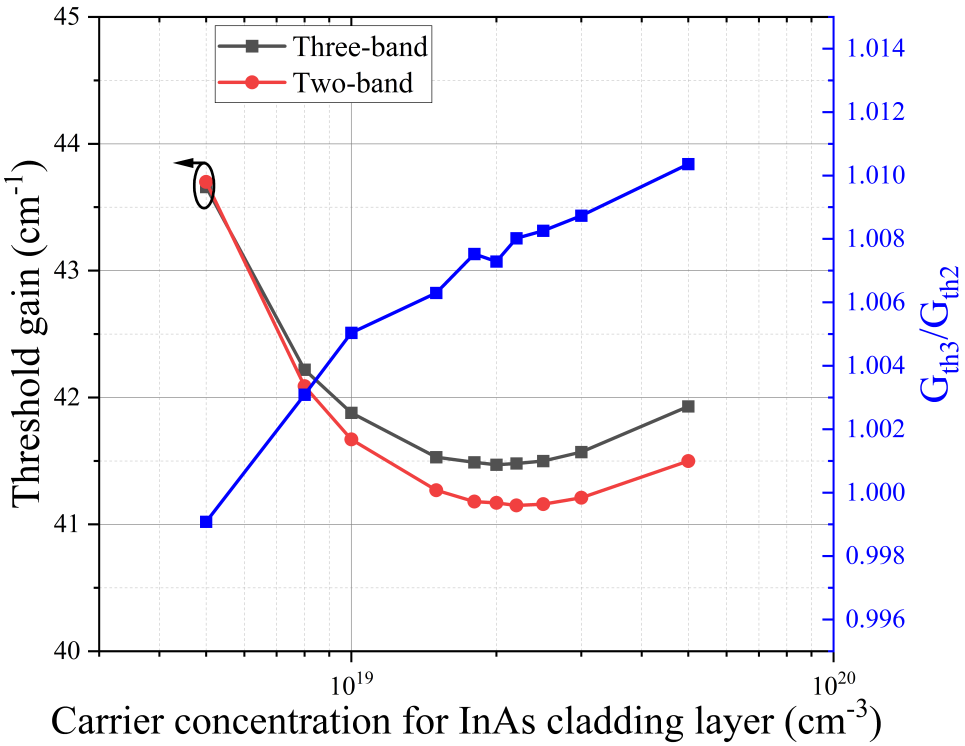

Figure 3.5: The calculated threshold gain as a function of carrier concentration for InAs cladding layer with a emission wavelength $\lambda = 4.6\mu$m. The blue curve represents the the difference between calculated threshold gain G_{th3}/G_{th2}.

compared to the two-band model. However, at $N = 10^{19}\text{cm}^{-3}$, the confinement factor of the three-band model is only 0.46% higher, but the absorption coefficient is 14.6% larger than that of the two-band model in Table 3.1. Therefore, when $N > 10^{18}\text{cm}^{-3}$, the threshold gain obtained from the three-band model exhibits a larger value compared to the two-band model in Figure 3.5. Although the threshold gain does not exhibit a linear increase, the relative difference between the two models increases almost linearly from -0.01% at $N = 5 \times 10^{18}\text{cm}^{-3}$ to 1.01% at $N = 5 \times 10^{19}\text{cm}^{-3}$.

When $N = 10^{18}\text{cm}^{-3}$, the two-band model displays a relatively higher threshold gain because the confinement factor needs to be obtained through solving the wavefunction, making the trend of threshold gain difficult to predict. Furthermore,

when $N < 2 \times 10^{19}\text{cm}^{-3}$, the threshold gain calculated shows a net decrease. However, after crossing this point, the threshold gain surges as the carrier concentration increases. The ICL waveguide is optimized at $N = 2.2 \times 10^{19}\text{cm}^{-3}$ for the two-band model with a threshold gain of 41.15cm^{-1} and at $N = 2 \times 10^{19}\text{cm}^{-3}$ for the three-band model with a threshold gain of 41.47cm^{-1}, as seen in Table 3.1. The carrier concentration for minimum threshold gain calculated from the two models has a deviation of 10%. The existence of a minimum threshold gain indicates that, at this point, the increase in the confinement factor compensates for the increase of loss from the increasing free carrier absorption.

This simplified model assumes a long cladding layer, preventing light from leaking into the substrate. As a result, the threshold gain exhibits a well-optimized point. However, thick layers also cause poor thermal dissipation and long growth time. The thickness of the layer will likely be reduced to 1µm for real cases, meaning that the light profile needs to consider the effect from the substrate and Ti/Au contact layer, causing the minimum threshold gain to shift. This delicate balance between numerous factors highlights the complex nature of designing and optimizing ICL waveguide structures and highlights the importance of selecting the appropriate model at different carrier concentration ranges.

3.2.2 High contrast Distributed Bragg Reflector

Other than the ICL design, which has a specific target wavelength, there are other applications, such as the Distributed Bragg Reflectors (DBRs)[19], [27] used for LED, that rely on the refractive index and absorption across a wider wavelength range. In these cases, having accurate index and absorption coefficient values to ensure optimal optical performance and efficiency across a broad spectrum is essential. The wavelength dependent index and absorption are illustrated in Figure

3.6, covering a wide wavelength range from 3 $\sim$ 24μm with $N = 1 \times 10^{19}\text{cm}^{-3}$, $5 \times 10^{18}\text{cm}^{-3}$, and $1 \times 10^{18}\text{cm}^{-3}$.

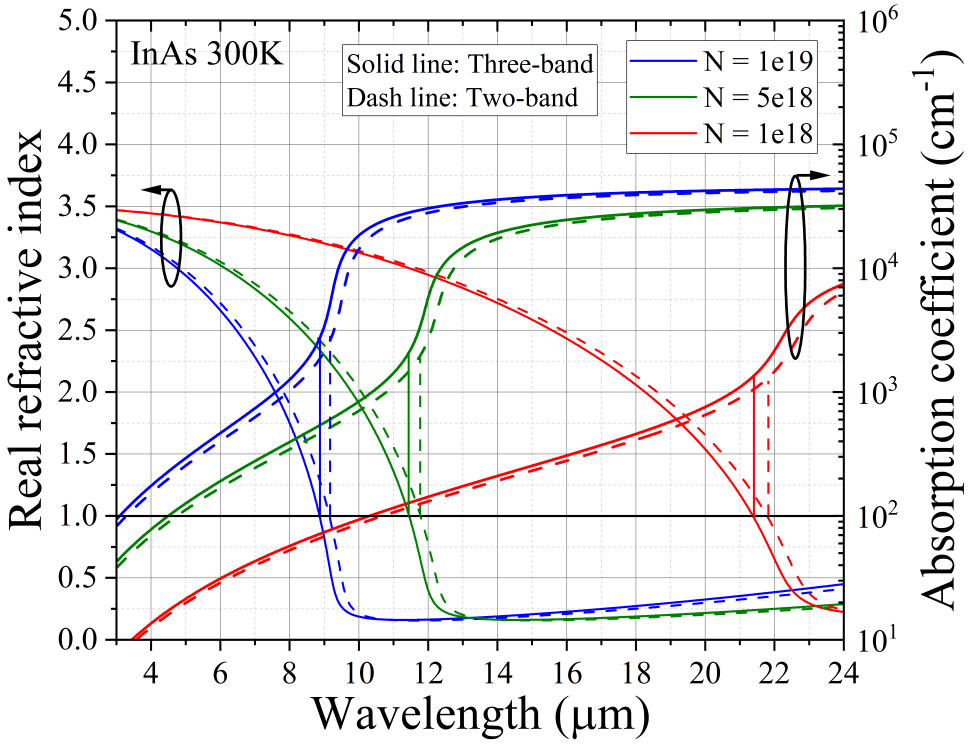

Figure 3.6: Refractive index and absorption coefficient as a function of wavelength for different carrier concentrations.

In Figure 3.6, the two-band model exhibits a slightly smaller index and larger free carrier absorption for specific wavelengths. If the imaginary part of the index is zero, the reflectance is zero when the index is equal to unity. The plasma wavelength is nearby the wavelength corresponding to a unity index. For n=1 (Black line in Figure 3.6), a longer wavelength is required for lower carrier concentrations. Simultaneously, the absorption coefficient decreases with the lower doping and longer wavelength. The index and absorption coefficient change rapidly for high carrier concentration but slowly for low carrier concentration and longer wavelength. Eventually, the absorption coefficient will saturate at a level of 10^4cm^{-1} for long wavelengths. High contrast DBRs are designed to achieve a high reflectance for

specific wavelengths, which are also desirable to have minimum free carrier loss. At short wavelengths, the free carrier absorption is strong, and the maximum reflectance is limited by the absorption. As a result, the consideration of the free carrier absorption limits the application for a high contrast DBR, such as the vertical surface emitting light-emitting diodes (LED) and photodetectors at shorter wavelengths.

For a specific carrier concentration, the two-band model exhibits a longer wavelength for n=1, this is because the two-band model has a larger effective mass, smaller plasma frequency and longer plasma wavelength than those of the three-band model. For $N = 1 \times 10^{19}\text{cm}^{-3}$, the associated wavelengths are $\lambda_2 = 9.18\mu\text{m}$ and $\lambda_3 = 8.85\mu\text{m}$ with a wavelength difference ratio of 3.7%. For $N = 5 \times 10^{18}\text{cm}^{-3}$, the associated wavelengths are $\lambda_2 = 11.83\mu\text{m}$ and $\lambda_3 = 11.43\mu\text{m}$ with the wavelength difference ratio of 3.4%. For $N = 1 \times 10^{18}\text{cm}^{-3}$, the associated wavelengths are $\lambda_2 = 21.85\mu\text{m}$ and $\lambda_3 = 21.42\mu\text{m}$ with the wavelength difference ratio of 2.0%. Although the index and absorption coefficient from the two models converge at shorter or longer wavelengths, they vary significantly around the plasma frequency. The absorption near the plasma frequency for the two models with n=1 is almost same. Thus, the primary challenge lies in the wavelength shift towards the target wavelength at short wavelengths. At shorter wavelengths, the wavelength difference ratio between two models is large. This is because of the difference in effective mass for the two bands in high carrier concentrations.

For short wavelength DBR design, high doping is required to have a small index around the designed wavelength. In this range, the effective mass from both models deviates from the experiment data. The measured value exhibits a large effective mass, which results in a small plasma frequency and longer plasma wavelength. Therefore, researchers need to consider about the effect of the wavelength red shift and may require an even higher doping level for better performance.

3.2.3 Reflectance Measurement

The reflectance measurement is an important method for determining the plasma frequency, and subsequently, the effective mass. By considering into account the carrier dependent effective mass and mobility, this technique can also be used to calculate the carrier concentration inside a the semiconductor. This approach enables researchers determine the carrier concentration without the possibility of damaging the sample, unlike Hall measurements. However, in order to find accurate carrier concentrations, an accurate index model for the plasma frequency is critical.

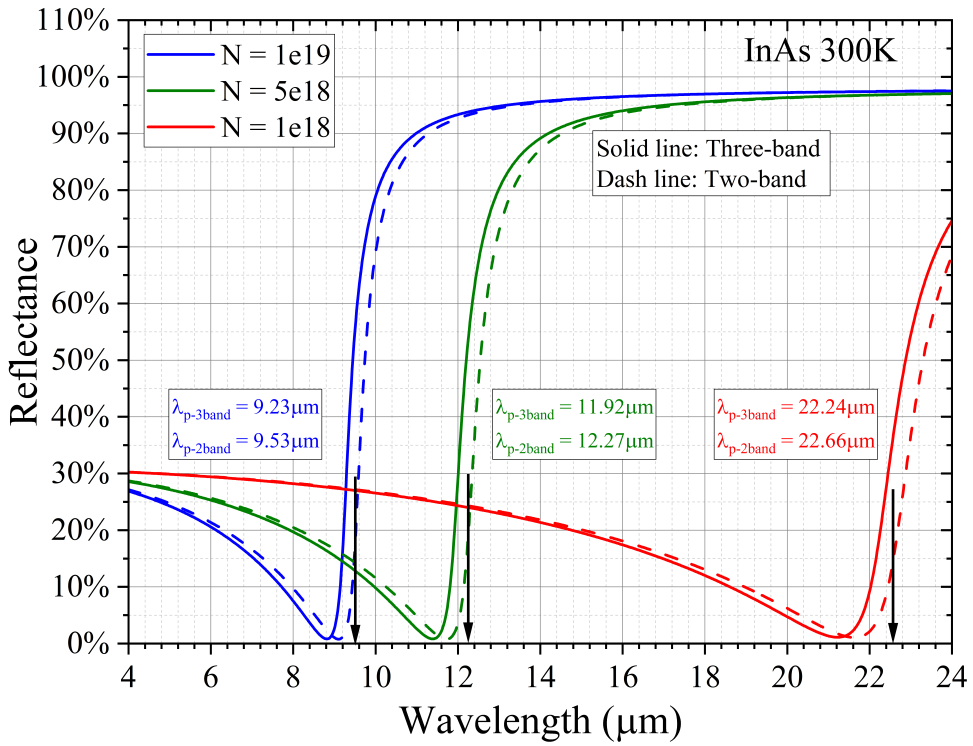

Figure 3.7: Refractive index and absorption coefficient as a function of wavelength for different carrier concentrations.

Figure 3.7, depicts the calculated reflectance as a function of wavelength based on Eq.(2.17) using input parameters calculated based on both the two-band (dashed) and the three-band (solid) models for three different carrier concentrations (blue, green, and red). In this figure, it is observed that the absolute value of the difference in the wavelength between the plasma frequency ω_p and the frequency of minimum reflectance ω_{min} increases as the carrier concentration decreases at longer wavelength. Nevertheless, the ω_p/ω_{min} ratio is small for low carrier concentrations, primarily due to the reduced damping in Figure 2.4. The typical value for ω_p/ω_{min} is approximately 0.96 for strong γ in high carrier concentrations[40], [41].

The three-band model demonstrates a smaller plasma wavelength than those from the two-band model for identical carrier concentrations. For a carrier concentration of $N = 1 \times 10^{19}\text{cm}^{-3}$, the plasma wavelengths are estimated to be $\lambda_2 = 9.52\mu\text{m}$ and $\lambda_3 = 9.23\mu\text{m}$, with a relative wavelength difference of 3.1%. For $N = 5 \times 10^{18}\text{cm}^{-3}$, the plasma wavelengths are $\lambda_2 = 12.27\mu\text{m}$ and $\lambda_3 = 11.92\mu\text{m}$, with a relative wavelength difference of 2.9%. For $N = 1 \times 10^{18}\text{cm}^{-3}$, the plasma wavelengths are $\lambda_2 = 22.66\mu\text{m}$ and $\lambda_3 = 21.24\mu\text{m}$, with a relative wavelength difference of 1.8%. Consequently, the relative plasma wavelength differences are small at low carrier concentration but large at high carrier concentrations. The plasma frequency shift ratio ω_p/ω_{min} for the two models are nearly identical and the difference is negligible.

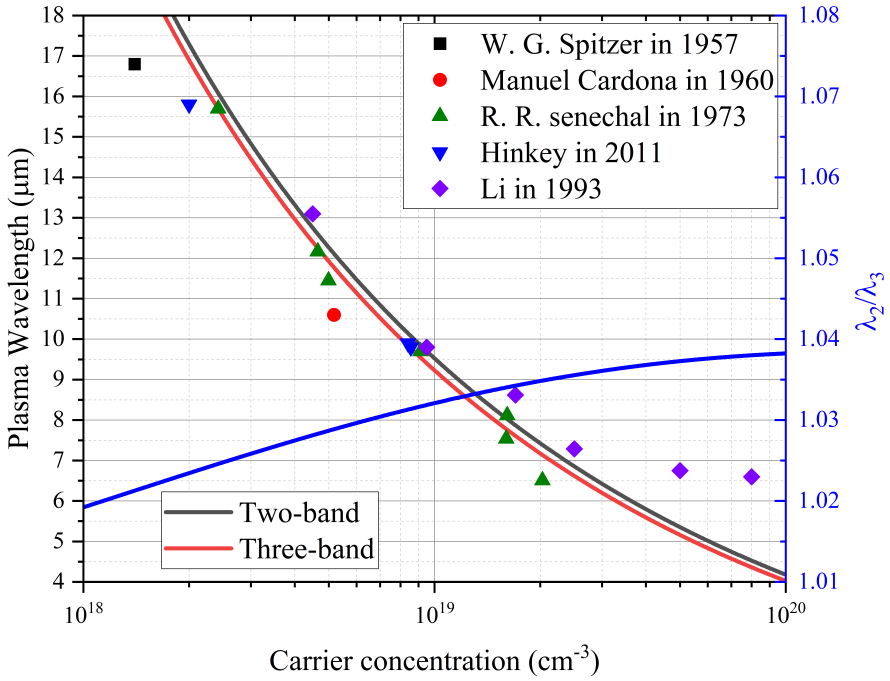

Figure 3.8: The relationship between wavelength and carrier concentration is connected through the plasma wavelength calculated by the two models. The black curve is from the two-band model and red curve is based on the three-band model. Also shown as experimentally measured values from several groups. [7], [10], [23], [36], [37]

Figure 3.8 provides a more intuitive picture of carrier concentration calculated from plasma wavelength and also considers experimentally measured values from several groups. The two-band model exhibits a higher carrier concentration for specific wavelengths. The difference in carrier concentration calculated from the two models is depicted with a blue curve. The carrier concentration calculated from the two-band model is 2% larger at $N = 10^{18}\text{cm}^{-3}$, and 3.8% in $N = 10^{20}\text{cm}^{-3}$. The experimental data show a good trend with simulation. However, when $\lambda < 7\mu\text{m}$, the measured plasma frequency exhibited a higher carrier concentration, when the corresponding $N > 3 \times 10^{19}\text{cm}^{-3}$, which is the range that the measured effective mass deviates from the simulation results. It is worth noting that the measured

plasma wavelength is shorter than the actual plasma wavelength. Thus, when $\lambda > 13\mu m$, the deviation from ω_p/ω_{min} makes the three-band model closer to the measured data. Fitting the measured reflectance spectrum with the simulation results can get a more accurate plasma frequency.

Chapter 4
Summary

This work provides a comprehensive assessment of the optical properties of bulk InAs based on two band structure models across a wide range of carrier concentrations and wavelengths. This study may help in the optimization of designed doped semiconductors for various optical applications. Both the two-band and three-band models yield satisfactory results at low carrier concentrations. However, at high carrier concentrations, the discrepancy between the two models leads to differences in refractive index and free carrier absorption calculations.

The influences of the two models are quantitatively discussed in the context of three applications: plasmon cladding layers for ICLs, DBRs, and plasma frequency measurements. The difference between the two models could affect the determination of device design parameters and the accuracy of measurements. The limitations of the $\mathrm{K} \cdot \mathrm{P}$ method arise at high carrier concentration, where remote bands may have substantial impact on the band structure, resulting in a higher increase in effective mass than the simulations based on the two simplified band models. Typically, it occurs when $\lambda < 3\mu\mathrm{m}$ or at high carrier concentrations when $N > 3 \times 10^{19}\mathrm{cm}^{-3}$. In this region, one should be more cautions about selecting models, and consider the designing such structures based on measured results. Overall, the choice of model should be based on the wavelength, carrier concentration range, and other factors associated with specific applications in mind.

Bibliography

[1] R. Q. Yang, "Infrared laser based on intersubband transitions in quantum wells," *Superlattices and Microstructures*, vol. 17, no. 1, pp. 77–83, Jan. 1995. DOI: 10.1006/spmi.1995.1017.

[2] J. Meyer, W. Bewley, C. Canedy, *et al.*, "The Interband Cascade Laser," *Photonics*, vol. 7, no. 3, p. 75, Sep. 2020. DOI: 10.3390/photonics7030075.

[3] I. Vurgaftman, R. Weih, M. Kamp, *et al.*, "Interband cascade lasers," *Journal of Physics D: Applied Physics*, vol. 48, no. 12, p. 123 001, Mar. 2015. DOI: 10.1088/0022-3727/48/12/123001.

[4] J. Koeth, R. Weih, M. O. Fischer, *et al.*, "Mid infrared DFB interband cascade lasers," M. Strojnik and M. S. Kirk, Eds., Aug. 2017. DOI: 10.1117/12.2277698.

[5] J. Scheuermann, P. Kluczynski, K. Siembab, *et al.*, "Interband Cascade Laser Arrays for Simultaneous and Selective Analysis of C1–C5 Hydrocarbons in Petrochemical Industry," *Applied Spectroscopy*, vol. 75, no. 3, pp. 336–342, Jan. 2021. DOI: 10.1177/0003702820978230.

[6] I. Vurgaftman, J. Meyer, and L. Ram-Mohan, "Mid-IR vertical-cavity surface-emitting lasers," *IEEE Journal of Quantum Electronics*, vol. 34, no. 1, pp. 147–156, 1998. DOI: 10.1109/3.655018.

[7] R. Q. Yang, L. Li, W. Huang, *et al.*, "InAs-Based Interband Cascade Lasers," *IEEE Journal of Selected Topics in Quantum Electronics*, vol. 25, no. 6, pp. 1–8, Nov. 2019. DOI: 10.1109/jstqe.2019.2916923.

[8] I. Vurgaftman, W. W. Bewley, C. L. Canedy, *et al.*, "Mid-IR type-II Interband Cascade Lasers," *IEEE Journal of Selected Topics in Quantum Electronics*, vol. 17, no. 5, pp. 1435–1444, Sep. 2011. DOI: 10.1109/jstqe.2011.2114331.

[9] J. A. Massengale, Y. Shen, R. Q. Yang, S. D. Hawkins, and J. F. Klem, "Long wavelength interband cascade lasers," *Applied Physics Letters*, vol. 120, no. 9, p. 091 105, Feb. 2022. DOI: 10.1063/5.0084565.

[10] R. T. Hinkey, Z. Tian, R. Q. Yang, T. D. Mishima, and M. B. Santos, "Reflectance spectrum of plasmon waveguide interband cascade lasers and observation of the Berreman effect," *Journal of Applied Physics*, vol. 110, no. 4, p. 043 113, Aug. 2011. DOI: 10.1063/1.3627172.

[11] L. Li, H. Ye, Y. Jiang, *et al.*, "MBE-grown long-wavelength interband cascade lasers on InAs substrates," *Journal of Crystal Growth*, vol. 425, pp. 369–372, Sep. 2015. DOI: 10.1016/j.jcrysgro.2015.02.016.

[12] R. Q. Yang, "InAs-based quantum cascade lasers with enhanced confinement," *Semiconductor Science and Technology*, vol. 30, no. 10, p. 105 023, Sep. 2015. DOI: 10.1088/0268-1242/30/10/105023.

[13] J. A. Massengale, Y. Shen, R. Q. Yang, S. D. Hawkins, and J. F. Klem, "Enhanced performance of InAs-based interband cascade lasers emitting between 10–13 µm," *Semiconductor Science and Technology*, vol. 38, no. 2, p. 025 009, Dec. 2022. DOI: 10.1088/1361-6641/acac4e.

[14] W. L. L. T. Borca-Tasciuc D. Achimov, "Thermal conductivity of InAs/AlSb superlattice," *Microscale Thermophysical Engineering*, vol. 5, no. 3, pp. 225–231, Jul. 2001. DOI: 10.1080/108939501753222896.

[15] L. Li, Y. Jiang, H. Ye, *et al.*, "Low-threshold InAs-based interband cascade lasers operating at high temperatures," *Applied Physics Letters*, vol. 106, no. 25, p. 251 102, Jan. 2015. DOI: 10.1063/1.4922995.

[16] Z. Tian, R. Yang, T. Mishima, *et al.*, "InAs-based interband cascade lasers near 6 µm," *Electronics Letters*, vol. 45, no. 1, p. 48, 2009. DOI: 10.1049/el:20092779.

[17] Z. Tian, R. Yang, T. Mishima, M. Santos, and M. Johnson, "Plasmon-waveguide interband cascade lasers near 7.5 µm," *IEEE Photonics Technology Letters*, vol. 21, no. 21, pp. 1588–1590, Nov. 2009. DOI: 10.1109/lpt.2009.2030686.

[18] S. Law, R. Liu, and D. Wasserman, "Doped semiconductors with band-edge plasma frequencies," *Journal of Vacuum Science & Technology B*, vol. 32, no. 5, p. 052 601, Sep. 2014. DOI: 10.1116/1.4891170.

[19] M. Bergthold, D. Wasserman, and A. J. Muhowski, "Plasmon-enhanced distributed bragg reflectors," *Infrared Physics & Technology*, vol. 125, p. 104 236, Sep. 2022. DOI: 10.1016/j.infrared.2022.104236.

[20] S. Law, D. C. Adams, A. M. Taylor, and D. Wasserman, "Mid-infrared designer metals," *Optics Express*, vol. 20, no. 11, p. 12 155, May 2012. DOI: 10.1364/oe.20.012155.

[21] P. Drude, *Annalen der physik*, vol. 1 566;3 369, 1900.

[22] E. O. Kane, "Band structure of indium antimonide," *Journal of Physics and Chemistry of Solids*, vol. 1, no. 4, pp. 249–261, Jan. 1957. DOI: 10.1016/0022-3697(57)90013-6.

[23] Y. B. Li, R. A. Stradling, T. Knight, *et al.*, "Infrared reflection and transmission of undoped and si-doped InAs grown on GaAs by molecular beam epitaxy," *Semiconductor Science and Technology*, vol. 8, no. 1, pp. 101–111, Jan. 1993. DOI: 10.1088/0268-1242/8/1/017.

[24] M. Razeghi, *Fundamentals of Solid State Engineering*. Springer-Verlag GmbH, Aug. 2018, ISBN: 9783319757087.

[25] D. Caughey and R. Thomas, "Carrier mobilities in silicon empirically related to doping and field," *Proceedings of the IEEE*, vol. 55, no. 12, pp. 2192–2193, 1967. DOI: 10.1109/proc.1967.6123.

[26] A. N. Baranov, Personal Communication, 2010.

[27] A. Kamboj, L. Nordin, P. Petluru, A. J. Muhowski, D. N. Woolf, and D. Wasserman, "All-epitaxial guided-mode resonance mid-wave infrared detectors," *Applied Physics Letters*, vol. 118, no. 20, p. 201 102, May 2021. DOI: 10.1063/5.0047534.

[28] R. R. Senechal and J. C. Woolley, "Redetermination of the effective mass in heavily-doped n-type InAs," *Physica Status Solidi (b)*, vol. 59, no. 1, K35–K37, Sep. 1973. DOI: 10.1002/pssb.2220590148.

[29] M. Sotoodeh, A. H. Khalid, and A. A. Rezazadeh, "Empirical low-field mobility model for III–V compounds applicable in device simulation codes," *Journal of Applied Physics*, vol. 87, no. 6, pp. 2890–2900, Mar. 2000. DOI: 10.1063/1.372274.

[30] T. Taliercio, V. N. Guilengui, L. Cerutti, E. Tournié, and J.-J. Greffet, "Brewster "mode" in highly doped semiconductor layers: An all-optical technique to monitor doping concentration," *Optics Express*, vol. 22, no. 20, p. 24 294, Sep. 2014. DOI: 10.1364/oe.22.024294.

[31] I. Vurgaftman, J. R. Meyer, and L. R. Ram-Mohan, "Band parameters for III–V compound semiconductors and their alloys," *Journal of Applied Physics*, vol. 89, no. 11, pp. 5815–5875, Jan. 2001. DOI: 10.1063/1.1368156.

[32] Y. U. Peter and M. Cardona, *Fundamentals of Semiconductors Physics and Materials Properties*. Springer, 2010, ISBN: 9783642007101.

[33] R. Q. Yang and J. M. Xu, "Bound and quasibound states in leaky quantum wells," *Physical Review B*, vol. 46, no. 11, pp. 6969–6974, Sep. 1992. DOI: 10.1103/physrevb.46.6969.

[34] S. Adachi, *Physical Properties of III-V Semiconductor Compounds*. Wiley, Sep. 1992. DOI: 10.1002/352760281x.

[35] M. Levinshtein, S. Rumyantsev, and M. Shur, *Handbook Series on Semiconductor Parameters*. WORLD SCIENTIFIC. DOI: 10.1142/2046.

[36] W. G. Spitzer and H. Y. Fan, "Determination of Optical Constants and Carrier Effective Mass of Semiconductors," *Physical Review*, vol. 106, no. 5, pp. 882–890, Jan. 1957. DOI: 10.1103/physrev.106.882.

[37] M. Cardona, "Electron Effective Masses of InAs and GaAs as a Function of Temperature and Doping," *Physical Review*, vol. 121, no. 3, pp. 752–758, Feb. 1961. DOI: 10.1103/physrev.121.752.

[38] T. S. L. Kesamanly F. P., D. N. Nasledov, L. A. Nikolaeva, and M. N. Pivovarov, *Fiz. i Tekhn. Polupr*, vol. 2, 1, pp. 56–63, 1968.

[39] F. Köhl, "Method for determination of semiconductor parameters from infrared reflectance data," *Optics Communications*, vol. 2, no. 4, pp. 157–158, Sep. 1970. DOI: 10.1016/0030-4018(70)90003-9.

[40] T. S. Moss, T. D. F. Hawkins, and G. J. Burrell, "Use of plasma edge reflection measurements in the study of semiconductors," *Journal of Physics C: Solid State Physics*, vol. 1, no. 5, pp. 1435–1446, Oct. 1968. DOI: 10.1088/0022-3719/1/5/333.

[41] N. Gaur, "Longitudinal optical phonon-plasmon coupling in InSb and InAs," *Physica B+C*, vol. 82, no. 2, pp. 262–270, Apr. 1976. DOI: 10.1016/0378-4363(76)90188-1.